

1

2 **A natural mutation between SARS-CoV-2 and SARS-CoV determines**
3 **neutralization by a cross-reactive antibody**

4

5

6 Nicholas C. Wu^{1,2,*}, Meng Yuan^{3,*}, Sandhya Bangaru^{3,*}, Deli Huang^{4,*}, Xueyong Zhu³,
7 Chang-Chun D. Lee³, Hannah L. Turner³, Linghang Peng⁴, Linlin Yang⁴, David
8 Nemazee⁴, Andrew B. Ward^{3,§}, Ian A. Wilson^{3,5,§}

9

10

11 ¹ Department of Biochemistry, University of Illinois at Urbana-Champaign, Urbana, IL
12 61801, USA

13 ² Carl R. Woese Institute for Genomic Biology, University of Illinois at Urbana-Champaign,
14 Urbana, IL 61801, USA

15 ³ Department of Integrative Structural and Computational Biology, The Scripps Research
16 Institute, La Jolla, CA 92037, USA

17 ⁴ Department of Immunology and Microbiology, The Scripps Research Institute, La Jolla,
18 CA 92037, USA

19 ⁵ The Skaggs Institute for Chemical Biology, The Scripps Research Institute, La Jolla,
20 CA, 92037, USA

21

22 * These authors contributed equally to this work

23 § Correspondence: andrew@scripps.edu (A.B.W.) and wilson@scripps.edu (I.A.W.)

24 **ABSTRACT**

25 Epitopes that are conserved among SARS-like coronaviruses are attractive targets for
26 design of cross-reactive vaccines and therapeutics. CR3022 is a SARS-CoV neutralizing
27 antibody to a highly conserved epitope on the receptor binding domain (RBD) on the spike
28 protein that can cross-react with SARS-CoV-2, but with lower affinity. Using x-ray
29 crystallography, mutagenesis, and binding experiments, we illustrate that of four amino
30 acid differences in the CR3022 epitope between SARS-CoV-2 and SARS-CoV, a single
31 mutation P384A fully determines the affinity difference. CR3022 does not neutralize
32 SARS-CoV-2, but the increased affinity to SARS-CoV-2 P384A mutant now enables
33 neutralization with a similar potency to SARS-CoV. We further investigated CR3022
34 interaction with the SARS-CoV spike protein by negative-stain EM and cryo-EM. Three
35 CR3022 Fabs bind per trimer with the RBD observed in different up-conformations due to
36 considerable flexibility of the RBD. In one of these conformations, quaternary interactions
37 are made by CR3022 to the N-terminal domain (NTD) of an adjacent subunit. Overall, this
38 study provides insights into antigenic variation and potential for cross-neutralizing epitopes
39 on SARS-like viruses.

40 INTRODUCTION

41 The ongoing COVID-19 pandemic, which is caused by the new coronavirus SARS-CoV-
42 2, continues to escalate. Investigating the immunogenicity and antigenicity of SARS-CoV-
43 2 is of great importance for vaccine and therapeutic development. The major antigen of
44 coronavirus is the spike (S) glycoprotein, which is expressed as a homotrimer on the virus
45 surface. Since the S protein is essential for virus entry through engaging the host receptor
46 and mediating virus-host membrane fusion, many antibodies to the S protein are
47 neutralizing [1-12]. The S proteins of SARS-CoV-2 and SARS-CoV, which caused a global
48 outbreak in 2003, have an amino-acid sequence identity of around 77% [13] that leads to
49 differences in antigenicity in serology studies [14, 15]. Although a few monoclonal
50 antibodies have been discovered that can cross-neutralize SARS-CoV and SARS-CoV-2
51 [6, 7, 16, 17], they seem to be relatively rare in COVID-19 patients [1, 3, 4, 14]. Thus, the
52 molecular determinants that define the antigenic differences and similarities between
53 SARS-CoV-2 and SARS-CoV need further exploration.

54

55 CR3022 was previously isolated from a SARS survivor and neutralizes SARS-CoV [18],
56 CR3022 was recently found to also be a cross-reactive antibody that can bind to both
57 SARS-CoV-2 and SARS-CoV [19]. Our recent crystal structure demonstrated that CR3022
58 targets a highly conserved cryptic epitope on the receptor binding domain (RBD) of the S
59 protein [20]. The CR3022 epitope is exposed only when the RBD is in the “up” but not the
60 “down” conformation on the S protein [20]. A few SARS-CoV-2 antibodies from COVID-19
61 patients have also recently been shown to target the CR3022 epitope [12, 17, 21],
62 suggesting that it is an important site of vulnerability for the antibody response in SARS-
63 CoV-2 infection. Out of 28 residues in the CR3022 epitope, 24 are conserved between
64 SARS-CoV-2 and SARS-CoV, explaining the cross-reactive binding of CR3022. However,
65 CR3022 has a higher affinity to SARS-CoV than to SARS-CoV-2 (>100-fold difference),

66 and can neutralize SARS-CoV, but not SARS-CoV-2, in a live virus neutralization assay
67 [20]. Therefore, CR3022 provides a good case study to probe antigenic variation between
68 SARS-CoV-2 and SARS-CoV.

69

70 We therefore aimed to dissect the molecular basis underlying the difference in binding
71 affinity and neutralization potency of CR3022 to SARS-CoV-2 and SARS-CoV. The crystal
72 structure of SARS-CoV RBD in complex with CR3022 was determined to compare with
73 the corresponding SARS-CoV-2 RBD structure [20]. In combination of mutagenesis and
74 binding experiments, we demonstrate that a single amino-acid difference at residue 384
75 (SARS-CoV-2 numbering) between the RBDs of SARS-CoV-2 and SARS-CoV can fully
76 explain the affinity difference with CR3022. Moreover, CR3022 is now able to neutralize
77 SARS-CoV-2 P384A with a similar potency to SARS-CoV. We further investigated the
78 molecular recognition of CR3022 to the SARS-CoV-2 spike protein by electron microscopy
79 and found that rotational flexibility of the RBD resulted in antibody binding to different
80 variants of up-conformations of the RBD relative to the spike trimer. Our findings validate
81 the CR3022 epitope as an important site of vulnerability for a cross-neutralizing antibody
82 response. Throughout this study, residues on RBD are numbered according to SARS-
83 CoV-2 numbering unless otherwise stated.

84

85 **RESULTS**

86 **P384A increases binding affinity of SARS-CoV-2 RBD to CR3022**

87 The epitope of CR3022 in SARS-CoV-2 and SARS-CoV differs by four residues. We
88 aimed to determine whether amino-acid variants in these four non-conserved residues
89 influence the binding affinity of CR3022 to RBD. Four SARS-CoV-2 RBD mutants, namely
90 A372T, P384A, T430M, and H519N (SARS-CoV-2 numbering), were recombinantly
91 expressed and examined (Figure 1A). These mutants converted the amino-acid sequence

92 of the CR3022 epitope in the SARS-CoV-2 RBD to that of SARS-CoV at each of the four
93 non-conserved residues. While binding of CR3022 mutants A372T ($K_D = 66$ nM), T430M
94 ($K_D = 64$ nM), and H519N ($K_D = 60$ nM) was comparable to wild type (WT) SARS-CoV-2
95 RBD ($K_D = 68$ nM), binding of CR3022 to the P384A mutant ($K_D = 1.4$ nM) was greatly
96 increased (Figure 1B), akin now to that with the SARS-CoV RBD ($K_D = 1.0$ nM) [20]. Thus,
97 the difference in binding affinity of CR3022 to SARS-CoV-2 RBD versus SARS-CoV RBD
98 can be attributed due to a single amino-acid difference at residue 384.

99

100 **CR3022 neutralizes SARS-CoV-2 P384A but not WT**

101 While CR3022 can neutralize SARS-CoV [18, 20], multiple groups have shown that it does
102 not neutralize SARS-CoV-2 [3, 5, 20, 22]. One possibility is that the affinity of CR3022 to
103 SARS-CoV-2 RBD is not sufficient to confer neutralizing activity. To test this hypothesis,
104 we compared neutralization of SARS-CoV-2 WT and the P384A mutant by CR3022.
105 Consistent with previous studies [3, 5, 20, 22], CR3022 failed to neutralize SARS-CoV-2
106 WT (Figure 2). However, CR3022 is now able to neutralize the SARS-CoV-2 P384A
107 mutant at an IC_{50} of 3.2 μ g/ml, which is comparable to its neutralizing activity to SARS-
108 CoV (IC_{50} of 5.2 μ g/ml). This finding validates the CR3022 epitope as a neutralizing
109 epitope in both SARS-CoV-2 and SARS-CoV, provided that the antibody affinity can
110 surpass a threshold for detection of neutralization.

111

112 Previous studies have indicated IgG bivalent binding can play an important role in
113 mediating neutralization of SARS-CoV-2, since the neutralization potency for many
114 antibodies is much greater when expressed as IgG rather than Fab [21, 23]. Subsequently,
115 we also tested the neutralizing activity of CR3022 Fab. Interestingly, the CR3022 Fab
116 neutralized SARS-CoV-2 P384A mutant with an IC_{50} of 4.4 μ g/ml, which is similar to that
117 of CR3022 IgG (3.2 μ g/ml) (Figure 2). This result indicates that CR3022, unlike many other

118 SARS-CoV-2 antibodies [21, 23], does not act bivalently with the S proteins on the virus
119 surface and, hence, neutralization is more sensitive to Fab binding affinity.

120

121 **Sequence conservation of residue 384**

122 We then examined the sequence conservation of residue 384 in other SARS-related
123 coronaviruses (SARSr-CoV) strains. Most SARSr-CoV strains have Pro at residue 384,
124 as in SARS-CoV-2. Only those strains that are phylogenetically very close to SARS-CoV,
125 such as bat SARSr-CoV WIV1 and bat SARSr-CoV WIV16, have Ala at residue 384
126 (Figure 3A). Phylogenetic analysis implies that P384A emerged during the evolution of
127 SARSr-CoV in bats (Figure 3A), which is the natural reservoir of SARSr-CoV [24].
128 However, it is unclear whether the emergence of P384A is due to neutral drift or positive
129 selection in bats or other species. In addition, given that residue 384 is proximal to the S2
130 domain when the RBD is in the “down” conformation (Figure 3B), whether P384A can
131 modulate the conformational dynamics of the “up and down” configurations of the RBD in
132 the S trimer and influence the viral replication fitness will require additional studies.

133

134 **Crystal structure reveals the impact of P384A in CR3022 binding**

135 We further determined the x-ray structure of SARS-CoV RBD in complex with CR3022 to
136 2.7 Å resolution (Figure 4A, Supplementary Table 1, and Supplementary Figure 1). The
137 overall structure of CR3022 in complex with SARS-CoV RBD is similar to that with SARS-
138 CoV-2 RBD [20] (C α RMSD of 0.5 Å for 343 residues in the RBD and Fab variable domain,
139 cf. fig. S2A and B of [20]) (Supplementary Figure 2). Nonetheless, the CR3022 elbow
140 angles, which are distant from the antibody-antigen interface, differ in the two structures,
141 as we mutated the elbow region (as described in [25]) of CR3022 to promote crystallization
142 with SARS-CoV RBD. The conserved binding mode of CR3022 to SARS-CoV-2 RBD and

143 SARS-CoV RBD indicates that the difference in binding affinity of CR3022 between SARS-
144 CoV-2 RBD and SARS-CoV RBD is only due to a very subtle structural difference.

145

146 To investigate how P384 and A384 lead to differential binding of CR3022, we compared
147 the RBD structures from SARS-CoV and SARS-CoV-2 when bound with CR3022. The
148 RBDs have a C α RMSD of only 0.6 Å (0.7 Å for CR3022 epitope residues). At residue
149 384, the backbone of SARS-CoV-2 is further from CR3022, as compared to that of SARS-
150 CoV (Figure 4B). This difference in backbone positioning (~1.3 Å shift) affects the
151 interaction of the RBD with CR3022 V_H S96, which is encoded by IGHD3-10 gene segment
152 on CDR H3 [18, 20]. While CR3022 V_H S96 forms a hydrogen bond (H-bond) with the
153 T385 side chain in both SARS-CoV-2 RBD and SARS-CoV RBD, it can form a second H-
154 bond with the backbone amide of T385 in SARS-CoV RBD (Figure 4C), but not SARS-
155 CoV-2 RBD (Figure 4D). In addition, CR3022 V_H S96 adopts different side-chain rotamers
156 when binding to SARS-CoV-2 and to SARS-CoV. Consequently, V_H S96 can make an
157 intramolecular H-bond with V_H T31 when CR3022 binds to SARS-CoV RBD (Figure 4C),
158 but not to SARS-CoV-2 (Figure 4D). In summary, V_H S96 forms three H-bonds when
159 CR3022 binds to SARS-CoV RBD, as compared to only one when CR3022 binds to
160 SARS-CoV-2 RBD. This observation indicates why binding of CR3022 to the SARS-CoV
161 RBD is energetically more favorable than to the SARS-CoV-2 RBD.

162

163 **CR3022-bound SARS-CoV S protein exhibits a rare three-up conformation**

164 To understand the binding of CR3022 to the RBD in the context of the homotrimeric S
165 protein, we previously proposed a structural model where CR3022 could only access its
166 epitope on the S protein when at least two RBD are in the “up” conformation and the RBD
167 is rotated relative to its unliganded structure [20]. To further evaluate and expand on this
168 model, negative-stain electron microscopy (nsEM) was performed on CR3022 in complex

169 with a stabilized version of the SARS-CoV homotrimeric S protein (Figure 5A, see
170 Materials and Methods). The 3D nsEM reconstruction revealed that one SARS-CoV S
171 protein could simultaneously bind to three CR3022 Fabs, with all three RBDs in the “up”
172 conformation (Figure 5B). Consistent with the structural model that we previously
173 proposed [20], the CR3022-bound RBD was indeed rotated compared to that in the
174 unliganded S protein [26-28], such that, in this conformation, steric hinderance between
175 CR3022 and the N-terminal domain (NTD) is minimized.

176

177 While our results here demonstrate that CR3022 Fab could form a stable complex with
178 SARS-CoV S protein in a prefusion conformation, a recent study reported that prefusion
179 SARS-CoV-2 S protein fell apart upon binding to CR3022 Fab as indicated by cryo-EM
180 [29]. It should be noted that the three-up conformation is much more rarely observed than
181 the other RBD conformations (all-down, one-up, and two-up) in SARS-CoV by cryo-EM
182 [26-28], or SARS-CoV-2 by cryo-EM [30-32] and cryo-electron tomography [33, 34], and
183 could relate to differences in the stability of S trimers in SARS-CoV versus SARS CoV-2
184 when CR3022 is bound. Further studies will be required to investigate whether such a
185 difference between SARS-CoV-2 and SARS-CoV is related to stability differences in the
186 recombinant spike proteins, or to different dynamics of the RBD on the virus or infected
187 cells.

188

189 **RBD flexibility and quaternary interactions in CR3022-bound SARS-CoV S protein**

190 To address some of these issues, we performed cryo-EM analysis to interrogate the
191 binding of CR3022 to SARS-CoV S protein at higher resolution (Supplementary Figure 3
192 and Supplementary Table 2). Focused 3D classification yielded 4 different structural
193 classes with classes 2 and 4 being nearly identical at the given resolution (Figure 5C and
194 Supplementary Figure 4). Class 3 is the most similar to the model from nsEM, although

195 the total particle number for classes 2 and 4 together exceed that for class 3
196 (Supplementary Figure 4). In contrast, class 1 is the least represented. In classes 2 and
197 4, CR3022 also appears to make quaternary contacts with the NTD, as suggested by well-
198 defined density in the CR3022-NTD interface (Figure 5C). The moderate resolution (6 to
199 7 Å) of the reconstructions precludes atomic-level descriptions, but the framework region
200 of the CR3022 light chain in classes 2 and 4 is in close proximity to a loop region in NTD
201 corresponding to residues 106-110. In addition, the constant region of CR3022 appears
202 to contact residue D23 of NTD. Another important observation is that the Fab in class 2
203 and 4 would clash with the adjacent RBD if it were in the “down” conformation. So, for the
204 Fab to exist in this quaternary conformation, the adjacent RBD has to be in the “up”
205 conformation. To evaluate the different dispositions of the RBD in these structures, we
206 compared the cryo-EM structure of an apo form of the SARS-CoV S protein where one
207 RBD is the “up” conformation (PDB 6ACD) [35]. The RBD in classes 1 to 4 are rotated by
208 84.1°, 54.3°, -54.7°, and 53.7°, respectively, relative to the apo one-up conformation (see
209 Materials and Methods). Furthermore, the CR3022-bound RBD in class 2 and 4 is more
210 open than in the apo form (Supplementary Figure 5), demonstrating the rotational flexibility
211 of the RBD. In fact, RBD conformational flexibility has also been noted in an ACE2-bound
212 SARS-CoV S protein. Three different dispositions (1 to 3) of the RBD were observed in
213 ACE2-bound SARS-CoV S protein with RBD tilts relative to horizontal top surface of the
214 S trimer of 51.2°, 73.3° and 111.6° compared to 68.9° for the apo one-up structure [35].
215 Our classes 2 and 4 appear to be somewhat intermediate between dispositions 2 and 3
216 (Supplementary Figure 6), whereas the other classes differ from the RBD dispositions in
217 the ACE2-bound SARS-CoV S structures. However, despite the flexibility of CR3022-
218 bound RBD, bivalent binding of CR3022 to S protein does not seem to occur on the virus
219 surface since an IgG avidity effect was not observed in the neutralization assay (see
220 above, Figure 2). Overall, these structural analyses indicate that RBD rotational flexibility

221 and acquisition of quaternary interactions can play an important role in CR3022 interaction
222 with the S protein. CR3022 adds to the growing list of neutralization antibodies that can
223 utilize quaternary interactions for binding to the S protein [12, 36].

224

225 **DISCUSSION**

226 While it is now known that SARS-CoV and SARS-CoV-2 differ in antigenicity despite
227 relatively high sequence conservation [1, 3, 4, 14], there is a paucity of understanding of
228 the underlying molecular determinants of these antigenic changes and the structural
229 consequences of these differences. Through structural analysis of the CR3022-RBD
230 complex and mutagenesis experiments, we show that a single amino-acid substitution at
231 residue 384 contributes to an important antigenic difference in a highly conserved
232 (neutralizing) epitope between SARS-CoV-2 and SARS-CoV.

233

234 While CR3022 cannot neutralize SARS-CoV-2 WT in almost all studies [3, 5, 20, 22], it
235 can neutralize the SARS-CoV-2 P384A mutant. The K_D of CR3022 Fab to SARS-CoV-2
236 WT RBD is 68 nM, whereas to SARS-CoV-2 P384A RBD is 1 nM (Figure 1B-C), indicating
237 that the affinity threshold for neutralization of SARS-CoV-2 to this epitope is in the low nM
238 range. However, despite having a low nM affinity to SARS-CoV-2 P384A RBD, CR3022
239 only weakly neutralizes SARS-CoV-2 P384A with an IC_{50} of 3.2 $\mu\text{g/ml}$ and SARS-CoV with
240 an IC_{50} of 5.2 $\mu\text{g/ml}$. In contrast, antibodies with similar or less Fab binding affinity to other
241 RBD epitopes, such as the receptor binding site, can neutralize SARS-CoV-2 much more
242 efficiently. For example, previously characterized SARS-CoV-2 antibodies CC12.1 and
243 CC12.3, which have a K_D to SARS-CoV-2 RBD of 17 nM and 14 nM respectively,
244 neutralize SARS-CoV-2 at an IC_{50} of ~ 20 ng/ml [3, 37]. Of note, the K_D and IC_{50} of CC12.1
245 and CC12.3 were measured in the same manner as this study. The lack of correlation
246 between affinity and neutralizing activity is therefore not due to the difference in the assays

247 between studies. In fact, a previous study also demonstrated a lack of correlation between
248 RBD binding and neutralization for monoclonal antibodies [3]. Together, these
249 observations suggest that the affinity threshold for SARS-CoV-2 neutralization by RBD-
250 targeting antibodies may be epitope dependent. The difference in affinity threshold for
251 different epitopes is also likely to be related not only in the ability to block ACE2-binding
252 [3, 38], but also in antibody avidity where bivalent binding can cross-link different RBD
253 domains on the same or different spikes and, hence, substantially enhance binding and
254 neutralization [23].

255

256 Given the scale of the outbreak, SARS-CoV-2 may persist and circulate in humans for
257 years to come [39]. A number of SARS-CoV-2 vaccine candidates are currently under
258 clinical trials (https://clinicaltrials.gov/ct2/who_table) [40], which offer a potential solution
259 to alleviate the global health and socio-economic devastation brought by SARS-CoV-2.
260 However, whether SARS-CoV-2 can escape vaccine-induced immunity through antigenic
261 drift remains to be determined, although escape mutations to many monoclonal antibodies
262 have been tested *in vitro* [2]. Identification of the key residues that are responsible for
263 differences in antigenicity among SARS-CoV-2, SARS-CoV, and possibly other SARS-
264 related viruses, should provide a starting point to understand the potential for antigenic
265 drift in SARS-like coronaviruses. The ongoing efforts in SARS-CoV-2 antibody discovery
266 and structural characterization will therefore advance our molecular understanding of
267 antigenic variation in SARS-like CoVs, and consequences for vaccine and therapeutic
268 design, especially to cross-neutralizing epitopes.

269

270 **ACKNOWLEDGEMENTS**

271 We thank Henry Tien for technical support with the crystallization robot, Jeanne Matteson
272 for contribution to mammalian cell culture, Wenli Yu to insect cell culture, Robyn Stanfield

273 for assistance in data collection, and Chris Mok for pilot testing of the pseudovirus assay.
274 We are grateful to the staff of Stanford Synchrotron Radiation Laboratory (SSRL)
275 Beamline 12-2 for assistance. This work was supported by NIH R00 AI139445 (N.C.W.),
276 NIH R01 AI073148 (D.N.), the Bill and Melinda Gates Foundation OPP1170236 (A.B.W.
277 and I.A.W.) and NIH CHAVD UM1 AI44462 (A.B.W. and I.A.W.). Use of the SSRL, SLAC
278 National Accelerator Laboratory, is supported by the U.S. Department of Energy, Office of
279 Science, Office of Basic Energy Sciences under Contract No. DE-AC02-76SF00515. The
280 SSRL Structural Molecular Biology Program is supported by the DOE Office of Biological
281 and Environmental Research, and by the National Institutes of Health, National Institute
282 of General Medical Sciences (including P41GM103393).

283

284 **AUTHOR CONTRIBUTIONS**

285 N.C.W., M.Y., D.H., S.B., A.B.W and I.A.W. conceived and designed the study. N.C.W.,
286 M.Y., C.C.D.L. and S.B. expressed and purified the proteins. M.Y. performed biolayer
287 interferometry binding assays. N.C.W. and M.Y. performed the crystallization experiment
288 and X.Z. collected the X-ray data. M.Y. determined and refined the X-ray structures. S.B.
289 and H.L.T. performed the negative-stain electron microscopy. D.H., L.P., L.Y. and D.N.
290 performed the pseudovirus neutralization assay. N.C.W., M.Y., D.H., S.B., A.B.W. and
291 I.A.W. analyzed the data. N.C.W., M.Y. and I.A.W. wrote the paper and all authors
292 reviewed and edited the paper.

293

294 **DECLARATION OF INTERESTS**

295 The authors declare no competing interests.

296 **MATERIALS AND METHODS**

297 **Expression and purification of SARS-CoV RBD**

298 RBD (residues: 306-527) of the SARS-CoV spike (S) protein (GenBank: ABF65836.1) was
299 fused with an N-terminal gp67 signal peptide and a C-terminal His₆ tag, and cloned into a
300 customized pFastBac vector [41]. Recombinant bacmid DNA was generated using the
301 Bac-to-Bac system (Thermo Fisher Scientific). Baculovirus was generated by transfecting
302 purified bacmid DNA into Sf9 cells using FuGENE HD (Promega), and subsequently used
303 to infect suspension cultures of High Five cells (Thermo Fisher Scientific) at an MOI of 5
304 to 10. Infected High Five cells were incubated at 28 °C with shaking at 110 r.p.m. for 72 h
305 for protein expression. The supernatant was then concentrated using a 10 kDa MW cutoff
306 Centrimate cassette (Pall Corporation). SARS-CoV RBD protein was purified by Ni-NTA,
307 followed by size exclusion chromatography, and buffer exchanged into 20 mM Tris-HCl
308 pH 7.4 and 150 mM NaCl.

309

310 **Expression and purification of SARS-CoV spike**

311 The SARS-CoV spike construct (Tor2 strain) for recombinant spike protein expression
312 contains the mammalian-codon-optimized gene encoding residues 1-1190 of the spike
313 followed by a C-terminal T4 fibritin trimerization domain, a HRV3C cleavage site, 8x-His
314 tag and a Twin-strep tags subcloned into the eukaryotic-expression vector pαH. Residues
315 at 968 and 969 were replaced by prolines for generating stable spike proteins as described
316 previously [28]. The spike plasmid was transfected into FreeStyle 293F cells and cultures
317 were harvested at 6-day post-transfection. Proteins were purified from the supernatants
318 on His-Complete columns using a 250 mM imidazole elution buffer. The elution was buffer
319 exchanged to Tris-NaCl buffer (25 mM Tris, 500 mM NaCl, pH 7.4) before further
320 purification using Superose 6 increase 10/300 column (GE Healthcare). Protein fractions
321 corresponding to the trimeric spike proteins were collected and concentrated.

322

323 **Expression and purification of CR3022 Fab**

324 The CR3022 Fab heavy (GenBank: DQ168569.1) and light (GenBank: DQ168570.1)
325 chains were cloned into phCMV3. The plasmids were transiently co-transfected into
326 Expi293F cells at a ratio of 2:1 (HC:LC) using ExpiFectamine™ 293 Reagent (Thermo
327 Fisher Scientific) according to the manufacturer's instructions. The supernatant was
328 collected at 7 days post-transfection. The Fab was purified with a CaptureSelect™ CH1-
329 XL Pre-packed Column (Thermo Fisher Scientific) followed by size exclusion
330 chromatography. For crystallization, a VSRRLP variant of the elbow region was used to
331 reduce the conformational flexibility between the constant and variable domains [25].

332

333 **Crystallization and structural determination**

334 Purified CR3022 Fab with a VSRRLP modification in the elbow region and SARS-CoV
335 RBD were mixed at a molar ratio of 1:1 and incubated overnight at 4°C. The complex (7.5
336 mg/ml) was screened for crystallization using the 384 conditions of the JCSG Core Suite
337 (Qiagen) on our custom-designed robotic CrystalMation system (Rigaku) at Scripps
338 Research by the vapor diffusion method in sitting drops containing 0.1 µl of protein and
339 0.1 µl of reservoir solution. Optimized crystals were then grown in 2 M sodium chloride
340 and 10% PEG 6000 at 4°C. Crystals were grown for 7 days and then flash cooled in liquid
341 nitrogen. Diffraction data were collected at cryogenic temperature (100 K) at Stanford
342 Synchrotron Radiation Lightsource (SSRL) beamline 12-2 with a wavelength of 1.033 Å,
343 and processed with HKL2000 [42]. Structures were solved by molecular replacement
344 using PHASER [43] with PDB 6W41 for CR3022 Fab [20] and PDB 2AJF for SARS-CoV
345 RBD [44]. Iterative model building and refinement were carried out in COOT [45] and
346 PHENIX [46], respectively. Ramachandran statistics were calculated using MolProbity
347 [47].

348

349 **Negative-stain electron microscopy**

350 Six molar excess of CR3022 Fab (unmodified) was added to SARS-CoV spike protein 1
351 hour prior to direct deposition onto carbon-coated 400-mesh copper grids. The grids were
352 stained with 2 % (w/v) uranyl-formate for 90 seconds immediately following sample
353 application. Grids were imaged on Tecnai T12 Spirit at 120 keV with a 4k x 4k Eagle CCD.
354 Micrographs were collected using Legikon [48] and images were transferred to Appion
355 [49] for particle picking using a difference-of-Gaussians picker (DoG-picker) [50] and
356 generation of particle stacks. Particle stacks were further transferred to Relion [51] for 2D
357 classification followed by 3D classification to select good classes. Select 3D classes were
358 auto-refined on Relion and used for making figures using UCSF Chimera [52].

359

360 **Cryo-EM sample preparation**

361 SARS-CoV spike protein was incubated with six molar excess of CR3022 Fab for 2 h. 3.5
362 μL of the complex (0.9 mg/ml) was mixed with 0.5 μL of 0.04 mM lauryl maltose neopentyl
363 glycol (LMNG) solution immediately before sample deposition onto a 1.2/1.3 300-Gold grid
364 (EMS). The grids were plasma cleaned for 7 seconds using a Gatan Solarus 950 Plasma
365 system prior to sample deposition. Following sample application, grids were blotted for 3
366 seconds before being vitrified in liquid ethane using a Vitrobot Mark IV (Thermo Fisher).

367

368 **Cryo-EM data collection and processing**

369 Data collection was performed using a Talos Arctica TEM at 200 kV with a Gatan K2
370 Summit detector at a magnification of 36,000x, resulting in a 1.15 \AA pixel size. Total
371 exposure was split into 250 ms frames with a total cumulative dose of $\sim 50 \text{ e}^-/\text{\AA}^2$.
372 Micrographs were collected through Legikon software at a nominal defocus range of -0.4
373 μm to -1.6 μm and MotionCor2 was used for alignment and dose weighting of the frames

374 [48, 53]. Micrographs were transferred to CryoSPARC 2.9 for further processing [54]. CTF
375 estimations were performed using GCTF and micrographs were selected using the Curate
376 Exposures tool in CryoSPARC based on their CTF resolution estimates (cutoff 5 Å) for
377 downstream particle picking, extraction and iterative rounds of 2D classification and
378 selection [55]. Particles selected from 2D classes were transferred to Relion 3.1 for direct
379 C3 refinement, symmetry expansion of particles and iterative rounds of 3D focused
380 classification using spherical masks around the RBD and Fab [51]. Final subsets of clean
381 particles from 4 different classes were each refined with C1 symmetry. Figures were
382 generated using UCSF Chimera and UCSF Chimera X [52].

383

384 **Calculation of rotation angles**

385 Comparisons of subunit rotation angles among different structures were performed with a
386 software ‘Superpose’ in the CCP4 package [56, 57]. For each classified conformation, the
387 C α atoms of the RBD domain are superimposed to the equivalent atoms of the RBD in
388 “up”-conformation in a previously reported spike trimer cryoEM structure (PDB 6ACD) [35].
389 The rotation matrices generated by superposing each pair of structures with ‘Superpose’
390 were adopted to calculate the subunit rotation angle following the equation shown as
391 below:

$$392 \quad \theta = \cos^{-1} \frac{X_{11} + Y_{22} + Z_{33} - 1}{2}$$

393 where θ is the subunit rotation angle, X_{11} , Y_{22} , and Z_{33} represent the X_{11} , Y_{22} , and Z_{33}
394 values in the rotation matrix calculated for the superpose.

395

396 **Bi-layer interferometry binding assay**

397 Binding assays were performed by bi-layer interferometry (BLI) using an Octet Red
398 instrument (FortéBio) as described previously [58]. Briefly, His₆-tagged SARS-CoV RBD

399 proteins at 20 to 100 µg/ml in 1x kinetics buffer (1x PBS, pH 7.4, 0.01% BSA and 0.002%
400 Tween 20) were loaded onto Anti-Penta-HIS (HIS1K) biosensors and incubated with the
401 indicated concentrations of CR3022 Fab. The assay consisted of five steps: 1) baseline:
402 60 s with 1x kinetics buffer; 2) loading: 300 s with His₆-tagged S or RBD proteins; 3)
403 baseline: 60 s with 1x kinetics buffer; 4) association: 120 s with samples (Fab or IgG); and
404 5) dissociation: 120 s with 1x kinetics buffer. For estimating the exact K_D, a 1:1 binding
405 model was used.

406

407 **Pseudovirus neutralization assay**

408 Pseudovirus preparation and assay were performed as previously described [3]. Briefly,
409 MLV-gag/pol and MLV-CMV plasmids was co-transfected into HEK293T cells along with
410 full-length or P384A SARS-CoV-2 spike plasmids using Lipofectamine 2000 to produce
411 pseudoviruses competent for single-round infection. The supernatant containing MLV-
412 pseudotyped viral particles was collected at 48 hours post transfection, aliquoted and
413 frozen at -80°C until used. For each well in a 96-well half-area plate, 25 µl of virus was
414 immediately mixed with 25 µl of serially diluted IgG or Fab, and incubated for 1 hour at
415 37°C. For each well, 10,000 HeLa-hACE2 cells in 50 µl of media supplemented with 20
416 µg/ml dextran were added to the antibody-virus mixture. The 96-well half-area plate was
417 then incubated at 37°C. At 42 to 48 hours post-infection, HeLa-hACE2 cells were lysed
418 using 1x luciferase lysis buffer (25 mM Gly-Gly pH 7.8, 15 mM MgSO₄, 4 mM EGTA, and
419 1% Triton X-100). Luciferase intensity was then measured using Bright-Glo Luciferase
420 Assay System (Promega) according to the manufacturer's instructions. Percentage of
421 neutralization was calculated using the following equation:

$$422 \quad \% \text{ neutralization} = 100 \times \left(1 - \frac{\text{RULs of sample} - \text{Average RULs of Background}}{\text{Average of RULs of Virus only control} - \text{Average RULs of Background}} \right)$$

423

424 **DATA AVAILABILITY**

425 The X-ray coordinates and structure factors have been deposited to the RCSB Protein
426 Data Bank under accession code: 7JN5. The EM maps will be deposited in the Electron
427 Microscopy Data Bank (EMDB).

428

429 **REFERENCES**

- 430 1. Brouwer PJM, Caniels TG, van der Straten K, Snitselaar JL, Aldon Y, Bangaru S,
431 et al. Potent neutralizing antibodies from COVID-19 patients define multiple
432 targets of vulnerability. *Science*. 2020;369(6504):643-50. doi:
433 10.1126/science.abc5902.
- 434 2. Baum A, Fulton BO, Wloga E, Copin R, Pascal KE, Russo V, et al. Antibody
435 cocktail to SARS-CoV-2 spike protein prevents rapid mutational escape seen
436 with individual antibodies. *Science*. 2020;369(6506):1014-8. Epub 2020/06/17.
437 doi: 10.1126/science.abd0831. PubMed PMID: 32540904; PubMed Central
438 PMCID: PMC7299283.
- 439 3. Rogers TF, Zhao F, Huang D, Beutler N, Burns A, He W-t, et al. Isolation of
440 potent SARS-CoV-2 neutralizing antibodies and protection from disease in a
441 small animal model. *Science*. 2020;369(6506):956-63. doi:
442 10.1126/science.abc7520.
- 443 4. Ju B, Zhang Q, Ge J, Wang R, Sun J, Ge X, et al. Human neutralizing antibodies
444 elicited by SARS-CoV-2 infection. *Nature*. 2020;584(7819):115-9. Epub
445 2020/05/27. doi: 10.1038/s41586-020-2380-z. PubMed PMID: 32454513.
- 446 5. Chi X, Yan R, Zhang J, Zhang G, Zhang Y, Hao M, et al. A neutralizing human
447 antibody binds to the N-terminal domain of the Spike protein of SARS-CoV-2.
448 *Science*. 2020;368(6504):1274-8. doi: 10.1126/science.abc6952.
- 449 6. Wec AZ, Wrapp D, Herbert AS, Maurer D, Haslwanter D, Sakharkar M, et al.
450 Broad neutralization of SARS-related viruses by human monoclonal antibodies.
451 *Science*. 2020;369(6504):731-6. doi: 10.1126/science.abc7424.
- 452 7. Pinto D, Park YJ, Beltramello M, Walls AC, Tortorici MA, Bianchi S, et al. Cross-
453 neutralization of SARS-CoV-2 by a human monoclonal SARS-CoV antibody.
454 *Nature*. 2020;583(7815):290-5. Epub 2020/05/19. doi: 10.1038/s41586-020-
455 2349-y. PubMed PMID: 32422645.
- 456 8. Zost SJ, Gilchuk P, Case JB, Binshtein E, Chen RE, Nkolola JP, et al. Potently
457 neutralizing and protective human antibodies against SARS-CoV-2. *Nature*.
458 2020;584(7821):443-9. Epub 2020/07/16. doi: 10.1038/s41586-020-2548-6.
459 PubMed PMID: 32668443.

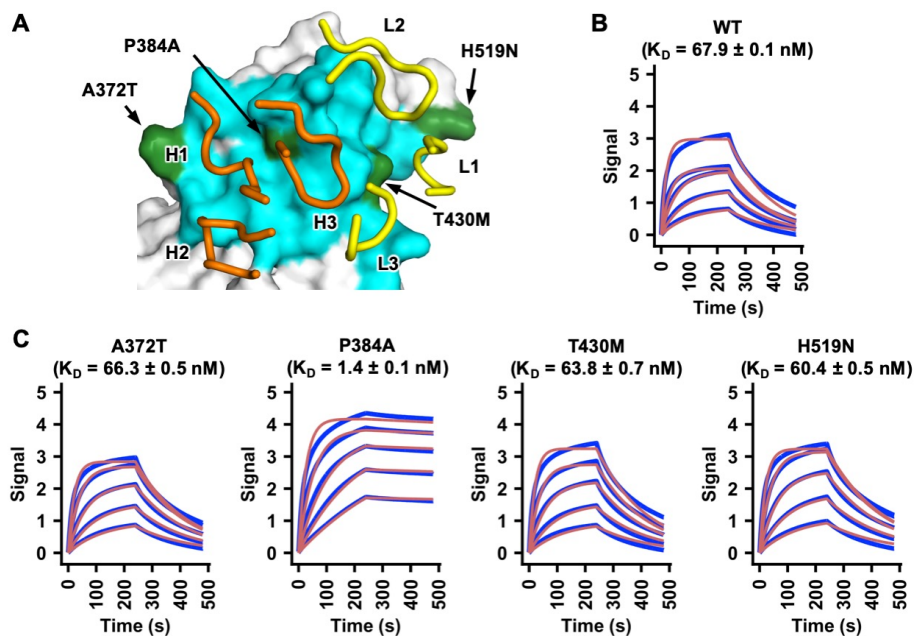
- 460 9. Cao Y, Su B, Guo X, Sun W, Deng Y, Bao L, et al. Potent neutralizing antibodies
461 against SARS-CoV-2 identified by high-throughput single-cell sequencing of
462 convalescent patients' B cells. *Cell*. 2020;182(1):73-84. Epub 2020/05/20. doi:
463 10.1016/j.cell.2020.05.025. PubMed PMID: 32425270; PubMed Central PMCID:
464 PMC7231725.
- 465 10. Seydoux E, Homad LJ, MacCamy AJ, Parks KR, Hurlburt NK, Jennewein MF, et
466 al. Analysis of a SARS-CoV-2-infected individual reveals development of potent
467 neutralizing antibodies with limited somatic mutation. *Immunity*. 2020;53(1):98-
468 105. doi: 10.1101/2020.05.12.091298.
- 469 11. Shi R, Shan C, Duan X, Chen Z, Liu P, Song J, et al. A human neutralizing
470 antibody targets the receptor binding site of SARS-CoV-2. *Nature*.
471 2020;584(7819):120-4. Epub 2020/05/27. doi: 10.1038/s41586-020-2381-y.
472 PubMed PMID: 32454512.
- 473 12. Liu L, Wang P, Nair MS, Yu J, Rapp M, Wang Q, et al. Potent neutralizing
474 antibodies directed to multiple epitopes on SARS-CoV-2 spike. *Nature*.
475 2020;584(7821):450-6. Epub 2020/07/23. doi: 10.1038/s41586-020-2571-7.
476 PubMed PMID: 32698192.
- 477 13. Zhou P, Yang XL, Wang XG, Hu B, Zhang L, Zhang W, et al. A pneumonia
478 outbreak associated with a new coronavirus of probable bat origin. *Nature*.
479 2020;579(7798):270-3. Epub 2020/02/06. doi: 10.1038/s41586-020-2012-7.
480 PubMed PMID: 32015507.
- 481 14. Lv H, Wu NC, Tsang OT-Y, Yuan M, Perera RAPM, Leung WS, et al. Cross-
482 reactive antibody response between SARS-CoV-2 and SARS-CoV infections.
483 *Cell Rep*. 2020;31(9):107725. doi: 10.1016/j.celrep.2020.107725.
- 484 15. Ou X, Liu Y, Lei X, Li P, Mi D, Ren L, et al. Characterization of spike glycoprotein
485 of SARS-CoV-2 on virus entry and its immune cross-reactivity with SARS-CoV.
486 *Nat Commun*. 2020;11(1):1620. Epub 2020/03/30. doi: 10.1038/s41467-020-
487 15562-9. PubMed PMID: 32221306; PubMed Central PMCID: PMC7100515.
- 488 16. Wang C, Li W, Drabek D, Okba NMA, van Haperen R, Osterhaus ADME, et al. A
489 human monoclonal antibody blocking SARS-CoV-2 infection. *Nat Commun*.
490 2020;11(1):2251. doi: 10.1101/2020.03.11.987958.
- 491 17. Zhou D, Duyvesteyn HME, Chen C-P, Huang C-G, Chen T-H, Shih S-R, et al.
492 Structural basis for the neutralization of SARS-CoV-2 by an antibody from a
493 convalescent patient. *Nat Struct Mol Biol*. 2020. doi: 10.1038/s41594-020-0480-
494 y.
- 495 18. ter Meulen J, van den Brink EN, Poon LL, Marissen WE, Leung CS, Cox F, et al.
496 Human monoclonal antibody combination against SARS coronavirus: synergy
497 and coverage of escape mutants. *PLoS Med*. 2006;3(7):e237. Epub 2006/06/27.
498 doi: 10.1371/journal.pmed.0030237. PubMed PMID: 16796401; PubMed Central
499 PMCID: PMC1483912.

- 500 19. Tian X, Li C, Huang A, Xia S, Lu S, Shi Z, et al. Potent binding of 2019 novel
501 coronavirus spike protein by a SARS coronavirus-specific human monoclonal
502 antibody. *Emerg Microbes Infect.* 2020;9(1):382-5. Epub 2020/02/18. doi:
503 10.1080/22221751.2020.1729069. PubMed PMID: 32065055.
- 504 20. Yuan M, Wu NC, Zhu X, Lee CD, So RTY, Lv H, et al. A highly conserved cryptic
505 epitope in the receptor-binding domains of SARS-CoV-2 and SARS-CoV.
506 *Science.* 2020;368(6491):630-3. Epub 2020/04/05. doi:
507 10.1126/science.abb7269. PubMed PMID: 32245784.
- 508 21. Liu H, Wu NC, Yuan M, Bangaru S, Torres JL, Caniels TG, et al. Cross-
509 neutralization of a SARS-CoV-2 antibody to a functionally conserved site is
510 mediated by avidity. *bioRxiv.* doi: 10.1101/2020.08.02.233536.
- 511 22. Yi C, Sun X, Ye J, Ding L, Liu M, Yang Z, et al. Key residues of the receptor
512 binding motif in the spike protein of SARS-CoV-2 that interact with ACE2 and
513 neutralizing antibodies. *Cell Mol Immunol.* 2020;17(6):621-30. Epub 2020/05/18.
514 doi: 10.1038/s41423-020-0458-z. PubMed PMID: 32415260; PubMed Central
515 PMCID: PMC7227451.
- 516 23. Barnes CO, West AP, Huey-Tubman KE, Hoffmann MAG, Sharaf NG, Hoffman
517 PR, et al. Structures of human antibodies bound to SARS-CoV-2 spike reveal
518 common epitopes and recurrent features of antibodies. *Cell.* 2020;182(4):828-42.
519 doi: 10.1016/j.cell.2020.06.025.
- 520 24. Li W, Shi Z, Yu M, Ren W, Smith C, Epstein JH, et al. Bats are natural reservoirs
521 of SARS-like coronaviruses. *Science.* 2005;310(5748):676-9. Epub 2005/10/01.
522 doi: 10.1126/science.1118391. PubMed PMID: 16195424.
- 523 25. Bailey LJ, Sheehy KM, Dominik PK, Liang WG, Rui H, Clark M, et al. Locking the
524 elbow: improved antibody Fab fragments as chaperones for structure
525 determination. *J Mol Biol.* 2018;430(3):337-47. Epub 2017/12/24. doi:
526 10.1016/j.jmb.2017.12.012. PubMed PMID: 29273204; PubMed Central PMCID:
527 PMC5800945.
- 528 26. Gui M, Song W, Zhou H, Xu J, Chen S, Xiang Y, et al. Cryo-electron microscopy
529 structures of the SARS-CoV spike glycoprotein reveal a prerequisite
530 conformational state for receptor binding. *Cell Res.* 2017;27(1):119-29. Epub
531 2016/12/23. doi: 10.1038/cr.2016.152. PubMed PMID: 28008928; PubMed
532 Central PMCID: PMC5223232.
- 533 27. Yuan Y, Cao D, Zhang Y, Ma J, Qi J, Wang Q, et al. Cryo-EM structures of
534 MERS-CoV and SARS-CoV spike glycoproteins reveal the dynamic receptor
535 binding domains. *Nat Commun.* 2017;8:15092. Epub 2017/04/11. doi:
536 10.1038/ncomms15092. PubMed PMID: 28393837; PubMed Central PMCID:
537 PMC5394239.
- 538 28. Kirchdoerfer RN, Wang N, Pallesen J, Wrapp D, Turner HL, Cottrell CA, et al.
539 Stabilized coronavirus spikes are resistant to conformational changes induced by
540 receptor recognition or proteolysis. *Sci Rep.* 2018;8(1):15701. Epub 2018/10/26.

- 541 doi: 10.1038/s41598-018-34171-7. PubMed PMID: 30356097; PubMed Central
542 PMCID: PMC6200764.
- 543 29. Huo J, Zhao Y, Ren J, Zhou D, Duyvesteyn HME, Ginn HM, et al. Neutralization
544 of SARS-CoV-2 by destruction of the prefusion spike. *Cell Host Microbe*. 2020.
545 Epub 2020/06/26. doi: 10.1016/j.chom.2020.06.010. PubMed PMID: 32585135;
546 PubMed Central PMCID: PMC7303615.
- 547 30. Wrapp D, Wang N, Corbett KS, Goldsmith JA, Hsieh CL, Abiona O, et al. Cryo-
548 EM structure of the 2019-nCoV spike in the prefusion conformation. *Science*.
549 2020;367(6483):1260-3. Epub 2020/02/23. doi: 10.1126/science.abb2507.
550 PubMed PMID: 32075877.
- 551 31. Walls AC, Park YJ, Tortorici MA, Wall A, McGuire AT, Velesler D. Structure,
552 function, and antigenicity of the SARS-CoV-2 spike glycoprotein. *Cell*.
553 2020;181(2):281-92.e6. Epub 2020/03/11. doi: 10.1016/j.cell.2020.02.058.
554 PubMed PMID: 32155444.
- 555 32. Cai Y, Zhang J, Xiao T, Peng H, Sterling SM, Walsh RM, Jr., et al. Distinct
556 conformational states of SARS-CoV-2 spike protein. *Science*. 2020. Epub
557 2020/07/23. doi: 10.1126/science.abd4251. PubMed PMID: 32694201.
- 558 33. Ke Z, Oton J, Qu K, Cortese M, Zila V, McKeane L, et al. Structures and
559 distributions of SARS-CoV-2 spike proteins on intact virions. *Nature*. 2020. doi:
560 10.1038/s41586-020-2665-2.
- 561 34. Yao H, Song Y, Chen Y, Wu N, Xu J, Sun C, et al. Molecular architecture of the
562 SARS-CoV-2 virus. *bioRxiv*. 2020. doi: 10.1101/2020.07.08.192104.
- 563 35. Song W, Gui M, Wang X, Xiang Y. Cryo-EM structure of the SARS coronavirus
564 spike glycoprotein in complex with its host cell receptor ACE2. *PLoS Pathog*.
565 2018;14(8):e1007236. Epub 2018/08/14. doi: 10.1371/journal.ppat.1007236.
566 PubMed PMID: 30102747; PubMed Central PMCID: PMC6107290.
- 567 36. Barnes CO, Jette CA, Abernathy ME, Dam K-MA, Esswein SR, Gristick HB, et al.
568 Structural classification of neutralizing antibodies against the SARS-CoV-2 spike
569 receptor-binding domain suggests vaccine and therapeutic strategies. *bioRxiv*.
570 2020. doi: 10.1101/2020.08.30.273920.
- 571 37. Yuan M, Liu H, Wu NC, Lee C-CD, Zhu X, Zhao F, et al. Structural basis of a
572 shared antibody response to SARS-CoV-2. *Science*. 2020;369(6507):1119-23.
573 doi: 10.1101/2020.06.08.141267. PubMed PMID: 32661058; PubMed Central
574 PMCID: PMC716439.
- 575 38. Tan CW, Chia WN, Qin X, Liu P, Chen MI, Tiu C, et al. A SARS-CoV-2 surrogate
576 virus neutralization test based on antibody-mediated blockage of ACE2-spike
577 protein-protein interaction. *Nat Biotechnol*. 2020;38:1073-8. Epub 2020/07/25.
578 doi: 10.1038/s41587-020-0631-z. PubMed PMID: 32704169.
- 579 39. Kissler SM, Tedijanto C, Goldstein E, Grad YH, Lipsitch M. Projecting the
580 transmission dynamics of SARS-CoV-2 through the postpandemic period.

- 581 Science. 2020;368(6493):860-8. Epub 2020/04/16. doi:
582 10.1126/science.abb5793. PubMed PMID: 32291278; PubMed Central PMCID:
583 PMC7164482.
- 584 40. Amanat F, Krammer F. SARS-CoV-2 vaccines: status report. *Immunity*.
585 2020;52(4):583-9. Epub 2020/04/08. doi: 10.1016/j.immuni.2020.03.007.
586 PubMed PMID: 32259480; PubMed Central PMCID: PMC7136867.
- 587 41. Ekiert DC, Friesen RH, Bhabha G, Kwaks T, Jongeneelen M, Yu W, et al. A
588 highly conserved neutralizing epitope on group 2 influenza A viruses. *Science*.
589 2011;333(6044):843-50. doi: 10.1126/science.1204839. PubMed PMID:
590 21737702; PubMed Central PMCID: PMC3210727.
- 591 42. Otwinowski Z, Minor W. Processing of X-ray diffraction data collected in
592 oscillation mode. *Methods Enzymol*. 1997;276:307-26. Epub 1997/01/01.
593 PubMed PMID: 27754618.
- 594 43. McCoy AJ, Grosse-Kunstleve RW, Adams PD, Winn MD, Storoni LC, Read RJ.
595 Phaser crystallographic software. *J Appl Crystallogr*. 2007;40(Pt 4):658-74. doi:
596 10.1107/S0021889807021206. PubMed PMID: 19461840; PubMed Central
597 PMCID: PMC2483472.
- 598 44. Li F, Li W, Farzan M, Harrison SC. Structure of SARS coronavirus spike
599 receptor-binding domain complexed with receptor. *Science*.
600 2005;309(5742):1864-8. Epub 2005/09/17. doi: 10.1126/science.1116480.
601 PubMed PMID: 16166518.
- 602 45. Emsley P, Lohkamp B, Scott WG, Cowtan K. Features and development of Coot.
603 *Acta Crystallogr D Biol Crystallogr*. 2010;66(Pt 4):486-501. doi:
604 10.1107/S0907444910007493. PubMed PMID: 20383002; PubMed Central
605 PMCID: PMC2852313.
- 606 46. Adams PD, Afonine PV, Bunkoczi G, Chen VB, Davis IW, Echols N, et al.
607 PHENIX: a comprehensive Python-based system for macromolecular structure
608 solution. *Acta Crystallogr D Biol Crystallogr*. 2010;66(Pt 2):213-21. Epub
609 2010/02/04. doi: 10.1107/S0907444909052925. PubMed PMID: 20124702;
610 PubMed Central PMCID: PMC2815670.
- 611 47. Chen VB, Arendall WB, 3rd, Headd JJ, Keedy DA, Immormino RM, Kapral GJ, et
612 al. MolProbity: all-atom structure validation for macromolecular crystallography.
613 *Acta Crystallogr D Biol Crystallogr*. 2010;66(Pt 1):12-21. doi:
614 10.1107/S0907444909042073. PubMed PMID: 20057044; PubMed Central
615 PMCID: PMC2803126.
- 616 48. Suloway C, Pulokas J, Fellmann D, Cheng A, Guerra F, Quispe J, et al.
617 Automated molecular microscopy: the new Legation system. *J Struct Biol*.
618 2005;151(1):41-60. Epub 2005/05/14. doi: 10.1016/j.jsb.2005.03.010. PubMed
619 PMID: 15890530.
- 620 49. Lander GC, Stagg SM, Voss NR, Cheng A, Fellmann D, Pulokas J, et al. Appion:
621 an integrated, database-driven pipeline to facilitate EM image processing. *J*

- 622 Struct Biol. 2009;166(1):95-102. PubMed PMID: 19263523; PubMed Central
623 PMCID: PMC2775544.
- 624 50. Voss NR, Yoshioka CK, Radermacher M, Potter CS, Carragher B. DoG Picker
625 and TiltPicker: software tools to facilitate particle selection in single particle
626 electron microscopy. J Struct Biol. 2009;166(2):205-13. PubMed PMID:
627 19374019; PubMed Central PMCID: PMC2768396.
- 628 51. Zivanov J, Nakane T, Forsberg BO, Kimanius D, Hagen WJ, Lindahl E, et al.
629 New tools for automated high-resolution cryo-EM structure determination in
630 RELION-3. eLife. 2018;7:e42166 Epub 2018/11/10. doi: 10.7554/eLife.42166.
631 PubMed PMID: 30412051; PubMed Central PMCID: PMC6250425.
- 632 52. Pettersen EF, Goddard TD, Huang CC, Couch GS, Greenblatt DM, Meng EC, et
633 al. UCSF Chimera--a visualization system for exploratory research and analysis.
634 J Comput Chem. 2004;25(13):1605-12. Epub 2004/07/21. doi:
635 10.1002/jcc.20084. PubMed PMID: 15264254.
- 636 53. Zheng SQ, Palovcak E, Armache JP, Verba KA, Cheng Y, Agard DA.
637 MotionCor2: anisotropic correction of beam-induced motion for improved cryo-
638 electron microscopy. Nat Methods. 2017;14(4):331-2. Epub 2017/03/03. doi:
639 10.1038/nmeth.4193. PubMed PMID: 28250466; PubMed Central PMCID:
640 PMC5494038.
- 641 54. Punjani A, Rubinstein JL, Fleet DJ, Brubaker MA. cryoSPARC: algorithms for
642 rapid unsupervised cryo-EM structure determination. Nat Methods.
643 2017;14(3):290-6. Epub 2017/02/07. doi: 10.1038/nmeth.4169. PubMed PMID:
644 28165473.
- 645 55. Zhang K. Gctf: Real-time CTF determination and correction. J Struct Biol.
646 2016;193(1):1-12. Epub 2015/11/26. doi: 10.1016/j.jsb.2015.11.003. PubMed
647 PMID: 26592709; PubMed Central PMCID: PMC4711343.
- 648 56. Winn MD, Ballard CC, Cowtan KD, Dodson EJ, Emsley P, Evans PR, et al.
649 Overview of the CCP4 suite and current developments. Acta Crystallogr D Biol
650 Crystallogr. 2011;67(Pt 4):235-42. Epub 2011/04/05. doi:
651 10.1107/S0907444910045749. PubMed PMID: 21460441; PubMed Central
652 PMCID: PMC3069738.
- 653 57. Krissinel E, Henrick K. Secondary-structure matching (SSM), a new tool for fast
654 protein structure alignment in three dimensions. Acta Crystallogr D Biol
655 Crystallogr. 2004;60(Pt 12 Pt 1):2256-68. Epub 2004/12/02. doi:
656 10.1107/S0907444904026460. PubMed PMID: 15572779.
- 657 58. Wu NC, Grande G, Turner HL, Ward AB, Xie J, Lerner RA, et al. In vitro evolution
658 of an influenza broadly neutralizing antibody is modulated by hemagglutinin
659 receptor specificity. Nat Commun. 2017;8:15371. doi: 10.1038/ncomms15371.
660 PubMed PMID: 28504265; PubMed Central PMCID: PMC5440694.
661
- 662



663

664 **Figure 1. A single P384A substitution increases CR3022 affinity to the SARS-CoV-2**

665 **RBD. (A)** Epitope residues on SARS-CoV RBD are colored in cyan and green. The

666 CR3022 CDR loops that contact the RBD are shown and labeled. Cyan: epitope residues

667 that are conserved between SARS-CoV-2 and SARS-CoV. Green: epitope residues that

668 are not conserved between SARS-CoV-2 and SARS-CoV. Orange: CR3022 heavy chain.

669 Yellow: CR3022 light chain. **(B-C)** Binding of CR3022 Fab to **(B)** wild-type (WT) SARS-

670 CoV-2 RBD and **(C)** different mutants was measured by biolayer interferometry with RBD

671 loaded on the biosensor and Fab in solution. Y-axis represents the response. Dissociation

672 constants (K_D) for the Fab were obtained using a 1:1 binding model, respectively, which

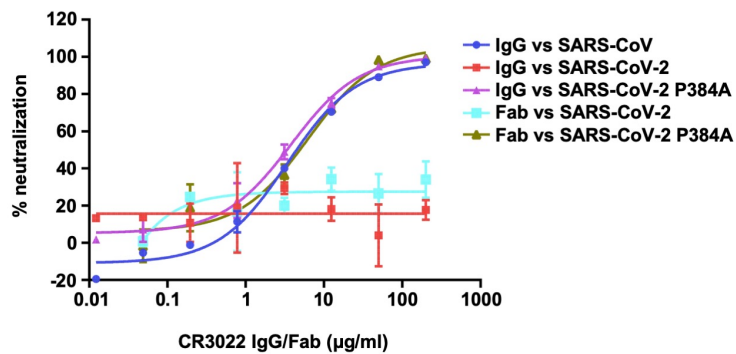
673 is represented by the red curves. Representative results of two replicates for each

674 experiment are shown. Of note, mammalian cell-expressed RBD was used in the binding

675 experiments in this study, whereas insect cell-expressed RBD was used in our previous

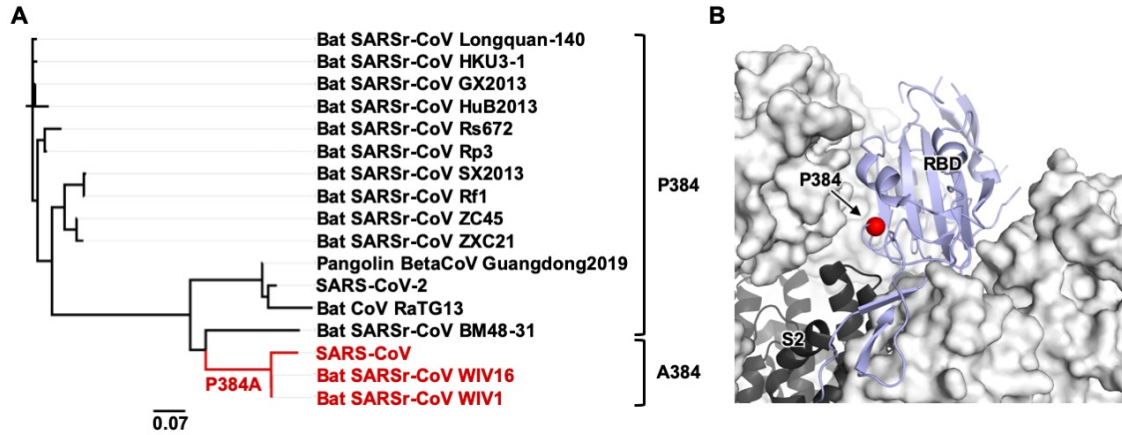
676 study [20]. This difference may explain the slight discrepancy in the K_D of CR3022 Fab to

677 SARS-CoV-2 RBD WT between this study and our previous study [20].



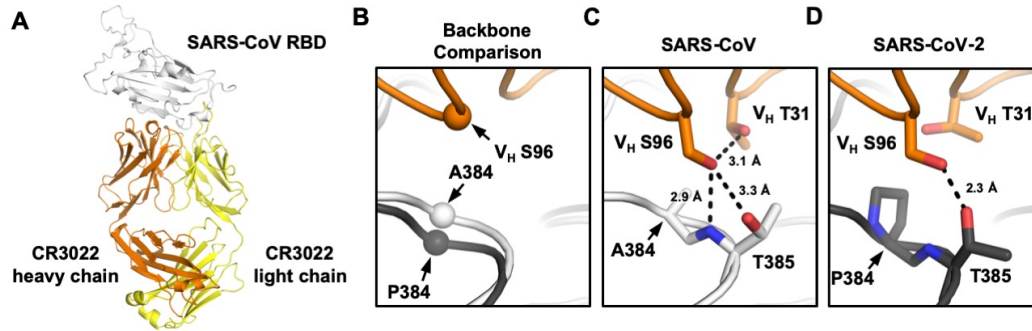
678

679 **Figure 2. Pseudovirus neutralization assay.** The neutralizing activity of CR3022 IgG or
680 Fab to SARS-CoV, SARS-CoV-2, and SARS-CoV-2 P384A mutant was measured in a
681 pseudovirus neutralization assay.



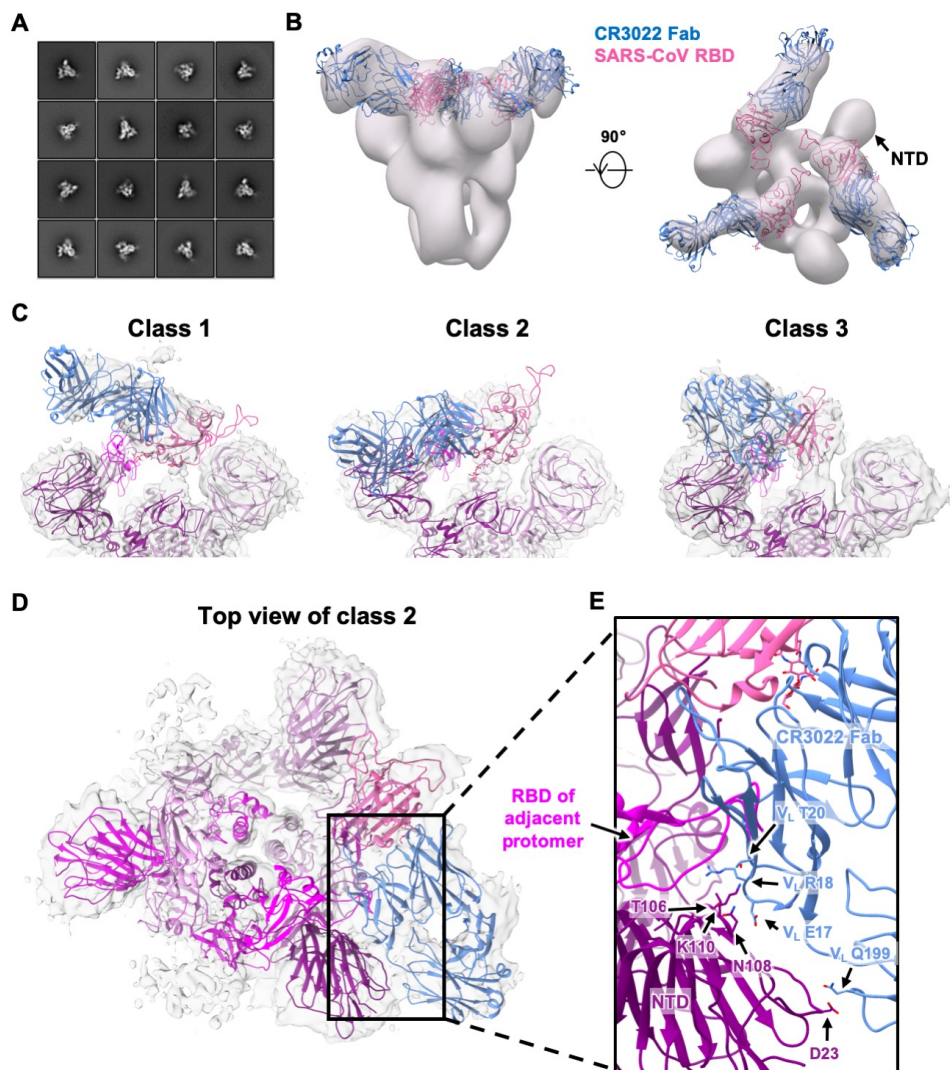
682

683 **Figure 3. Sequence conservation and location of residue 384.** (A) A phylogenetic tree
684 was constructed based on the amino-acid sequences of RBDs from SARS-CoV-2, SARS-
685 CoV, and SARS-related coronavirus (SARSr-CoV) strains. Branches corresponding to
686 strains that have A384 are colored in red on the phylogenetic tree. Scale bar represents
687 0.07 amino-acid substitutions per position. (B) The location of P384 is shown on the
688 SARS-CoV-2 S protein (PDB 6VXX [31]). S1 domain is represented by the white surface
689 and the S2 domain by the black cartoon. The location of residue 384 is indicated by the
690 red sphere on the RBD in the “down” conformation (blue cartoon).



691

692 **Figure 4. Crystal structure of CR3022 in complex with SARS-CoV RBD.** (A) Crystal
693 structure of CR3022 Fab in complex with SARS-CoV RBD. CR3022 heavy chain is colored
694 in orange, CR3022 light chain in yellow, and SARS-CoV-2 RBD in light grey. (B) Structures
695 of CR3022 in complex with SARS-CoV-2 RBD and with SARS-CoV RBD were aligned
696 using the CR3022 heavy chain variable domain and the region around residue 384 is
697 shown. Orange: CR3022 heavy chain. White: SARS-CoV RBD. Dark gray: SARS-CoV-2
698 RBD. The C α s of S96 on CR3022 heavy chain, A384 on SARS-CoV RBD, and P384 on
699 SARS-CoV-2 RBD are shown in sphere representation. (C-D) Interaction between
700 CR3022 and residue 384 on (C) SARS-CoV RBD, and (D) SARS-CoV-2 RBD. Hydrogen
701 bonds are represented by dashed lines.



702

703 **Figure 5. Negative-stain EM and cryo-EM analysis of SARS spike bound to CR3022**

704 **Fab. (A)** Representative 2D nsEM class averages of the trimeric SARS-CoV spike

705 glycoprotein complexed with three CR3022 Fabs. **(B)** Side and top view of the 3D

706 reconstruction showing CR3022 Fabs bound to all 3 RBDs on the SARS-CoV spike. The

707 SARS-CoV RBD-CR3022 complex from the crystal structure is fitted into the nsEM density

708 with the RBD shown in pink and CR3022 Fab in blue. **(C)** Side views of the B-factor-

709 sharpened cryo-EM maps (transparent gray surface representation) representing three

710 different classes of SARS spike with CR3022 Fab with different RBD-Fab orientations.

711 While four different classes were identified, only three classes are shown here because

712 classes 2 and 4 are very similar (Supplementary Figure 4). The RBD-Fab complex model
713 is fit into the densities with the RBDs shown in pink and CR3022 Fabs represented in blue.
714 The atomic model of the apo SARS-CoV spike (PDB 6ACD) [35] is also fit into density
715 with one RBD removed for clarity. The protomers are colored in purple, magenta and deep
716 magenta. **(D)** Top view of the class 2 cryo-EM map depicting potential quaternary contacts
717 between the RBD-bound Fab and the spike NTD in this conformation. In this RBD-Fab
718 conformation, the Fab would clash with the “down” RBD of the adjacent protomer
719 (magenta) and, therefore, the adjacent RBD can only exist in an “up” conformation. **(E)** A
720 close-up view of the Fab-spike interface showing the superimposition of CR3022 Fab and
721 adjacent RBD. The residues that can contribute to quaternary interactions between
722 CR3022 light chain and the NTD in two of the four classes (2 and 4) are shown.

Supplementary Table 1. X-ray data collection and refinement statistics.

Data collection	
Beamline	SSRL 12-2
Wavelength (Å)	0.97946
Space group	C 1 2 1
Unit cell parameters (Å and °)	a=265.7, b=59.9, c=51.7, β=99.8
Resolution (Å)	50.0–2.70 (2.76–2.70) ^a
Unique reflections	21,547 (2,021) ^a
Redundancy	6.7 (5.5) ^a
Completeness (%)	100.0 (100.0) ^a
<I/σ _I >	14.7 (1.0) ^a
R _{sym} ^b (%)	9.2 (86.1) ^a
R _{pim} ^b (%)	5.4 (54.8) ^a
CC _{1/2} ^c (%)	99.4 (74.4) ^a
Refinement statistics	
Resolution (Å)	45.0–2.70
Reflections (work)	21,501
Reflections (test)	1,011
R _{cryst} ^d / R _{free} ^e (%)	22.2 / 27.6
No. of atoms	4,872
Macromolecules	4,795
Glycans	42
Solvent	30
Average B-value (Å ²)	80
Macromolecules	80
RBD	104
Fab	70
Glycans	30
Solvent	60
Wilson B-value (Å ²)	64
RMSD from ideal geometry	
Bond length (Å)	0.005
Bond angle (°)	1.17
Ramachandran statistics (%)	
Favored	95.6
Outliers	0.16
PDB code	7JN5

^a Numbers in parentheses refer to the highest resolution shell.

^b $R_{sym} = \frac{\sum_{hkl} \sum_i |I_{hkl,i} - \langle I_{hkl} \rangle|}{\sum_{hkl} \sum_i I_{hkl,i}}$ and $R_{pim} = \frac{\sum_{hkl} (1/(n-1))^{1/2} \sum_i |I_{hkl,i} - \langle I_{hkl} \rangle|}{\sum_{hkl} \sum_i I_{hkl,i}}$, where $I_{hkl,i}$ is the scaled intensity of the *i*th measurement of reflection *h, k, l*, $\langle I_{hkl} \rangle$ is the average intensity for that reflection, and *n* is the redundancy.

^c CC_{1/2} = Pearson correlation coefficient between two random half datasets.

^d $R_{cryst} = \frac{\sum_{hkl} |F_o - F_c|}{\sum_{hkl} |F_o|} \times 100$, where F_o and F_c are the observed and calculated structure factors, respectively.

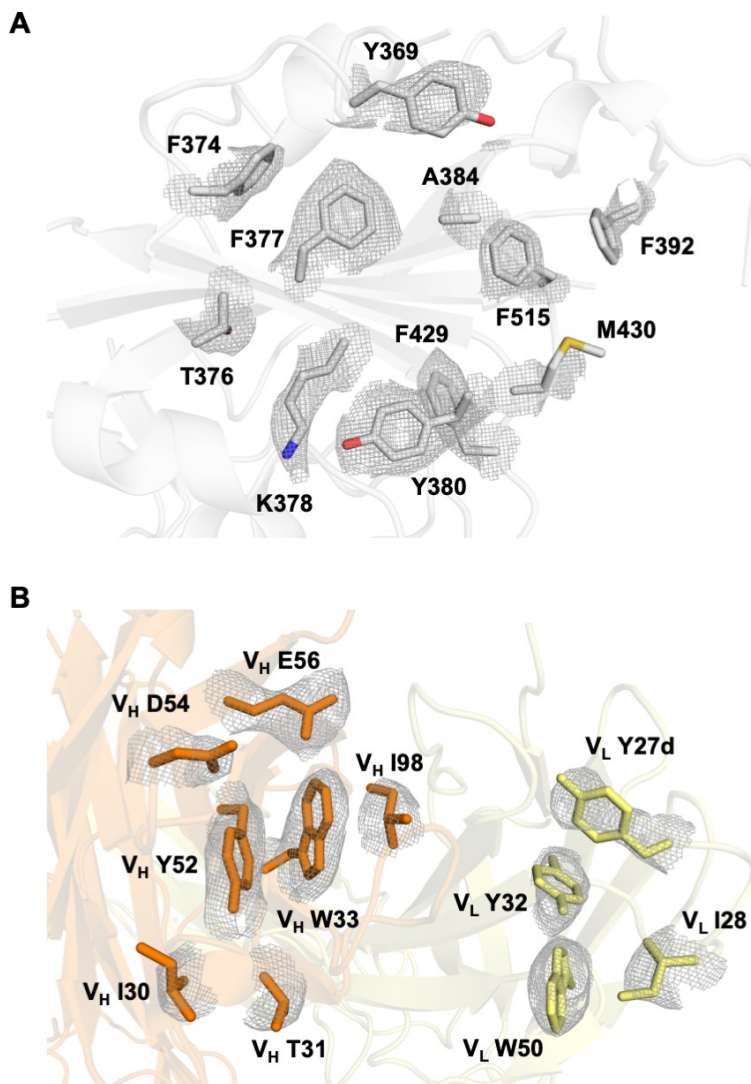
^e R_{free} was calculated as for R_{cryst} , but on a test set comprising 5% of the data excluded from refinement.

724

Supplementary Table 2. Cryo-EM data collection and refinement statistics.

Map	SARS-CR3022Fab Class 1	SARS-CR3022Fab Class 2	SARS-CR3022Fab Class 3	SARS-CR3022Fab Class 4
EMDB	Pending	Pending	Pending	Pending
Data collection				
Microscope	FEI Talos Arctica	FEI Talos Arctica	FEI Talos Arctica	FEI Talos Arctica
Voltage (kV)	200	200	200	200
Detector	Gatan K2 Summit	Gatan K2 Summit	Gatan K2 Summit	Gatan K2 Summit
Recording mode	Counting	Counting	Counting	Counting
Nominal magnification	36,000	36,000	36,000	36,000
Movie micrograph pixelsize (Å)	1.15	1.15	1.15	1.15
Dose rate (e ⁻ /[(camera pixel)*s])	5.6	5.6	5.6	5.6
Number of frames per movie micrograph	47	47	47	47
Frame exposure time (ms)	250	250	250	250
Movie micrograph exposure time (s)	11.7	11.7	11.7	11.7
Total dose (e ⁻ /Å ²)	50	50	50	50
Defocus range (µm)	-0.4 to -1.6	-0.4 to -1.6	-0.4 to -1.6	-0.4 to -1.6
EM data processing				
Number of movie micrographs	2952	2952	2952	2952
Number of molecular projection images in map	17,472	28,821	34,803	31,645
Symmetry	C1	C1	C1	C1
Map resolution (FSC 0.143; Å)	6.83	6.24	6.42	6.15
Map sharpening B-factor (Å ²)	-164.6	-147.4	-120.5	-138.1

725



726

727 **Supplementary Figure 1. X-ray electron density maps for epitope and paratope**

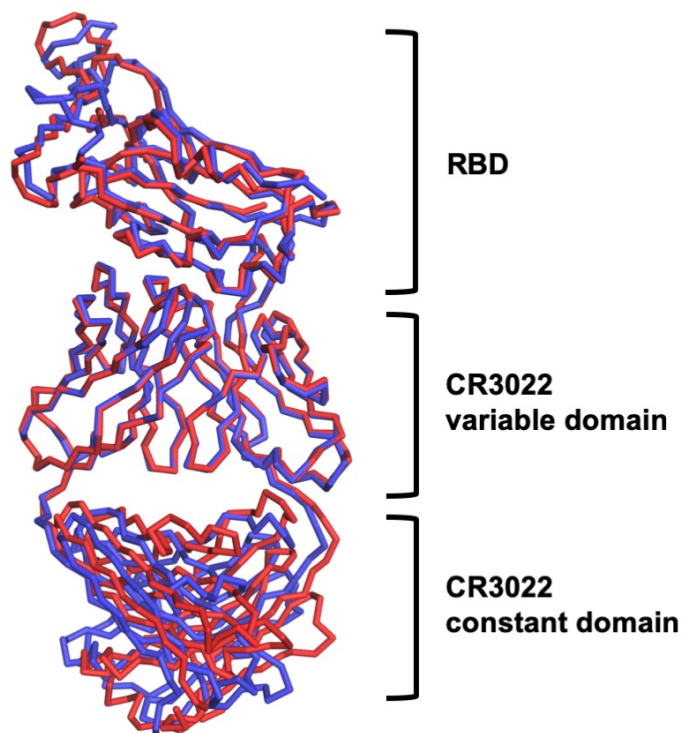
728 **regions of SARS CoV RBD with Fab CR3022. (A) Final 2Fo-Fc electron density maps**

729 **for the side chains in the epitope region of SARS-CoV-2 contoured at 1 σ . (B) Final 2Fo-**

730 **Fc electron density maps for the paratope region of CR3022 contoured at 1 σ . The heavy**

731 **chain is colored in orange, and light chain in yellow. Epitope and paratope residues are**

732 **labeled.**



733

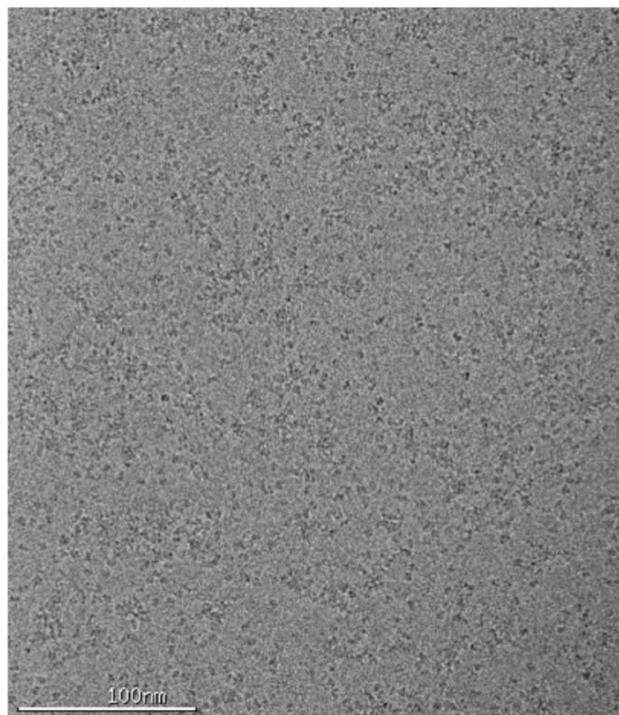
734 **Supplementary Figure 2. Structural alignment of CR3022-bound SARS-CoV RBD**

735 **and CR3022-bound SARS-CoV-2 RBD.** Structure of CR3022 in complex with SARS-CoV

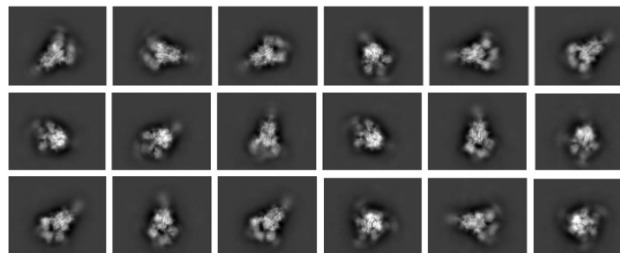
736 RBD (this study) is aligned to that with SARS-CoV-2 RBD (PDB 6W41). Structural

737 alignment was performed using CR3022 heavy chain variable domain. Red: CR3022 in

738 complex with SARS-CoV RBD. Blue: CR3022 in complex with SARS-CoV-2 RBD.

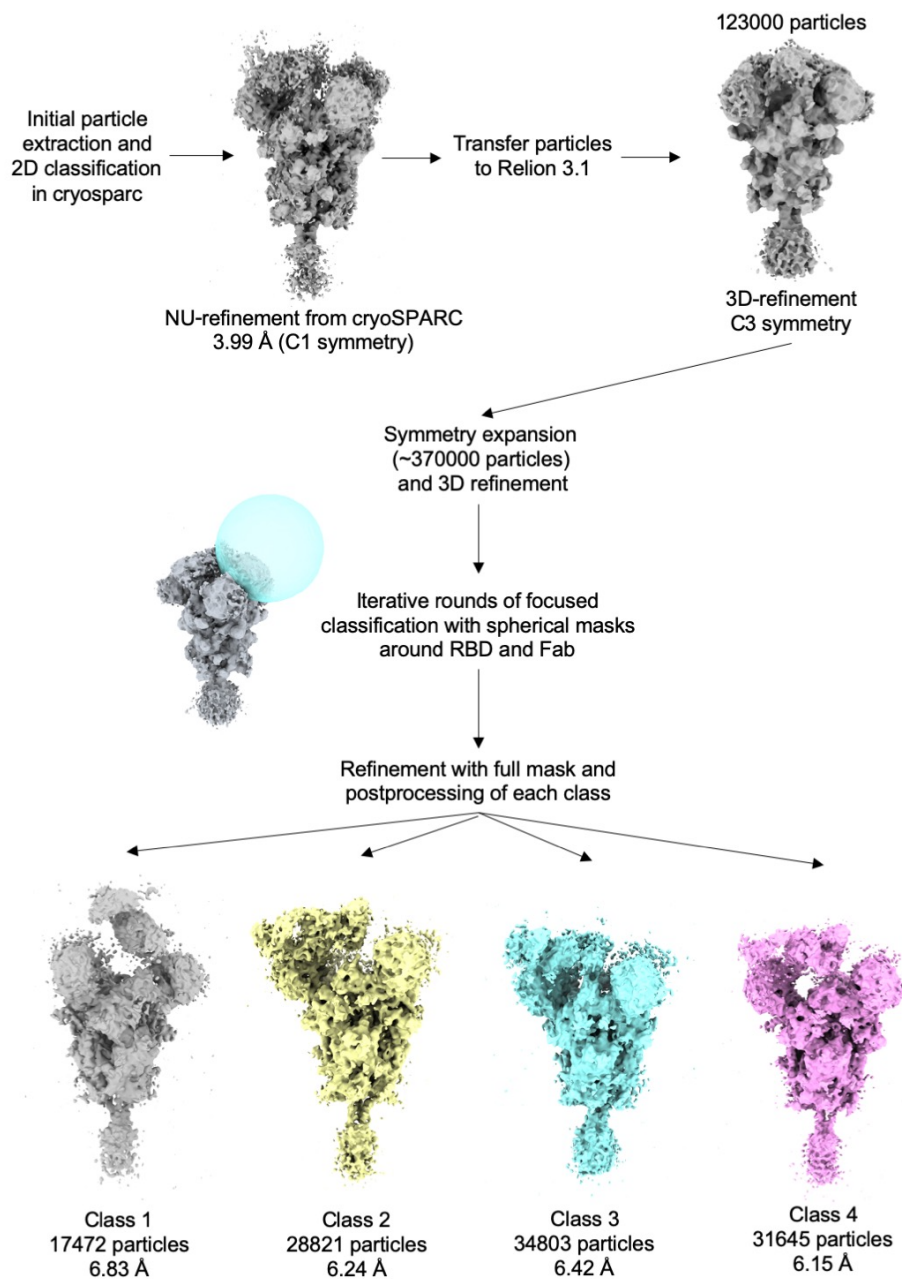


2D class averages



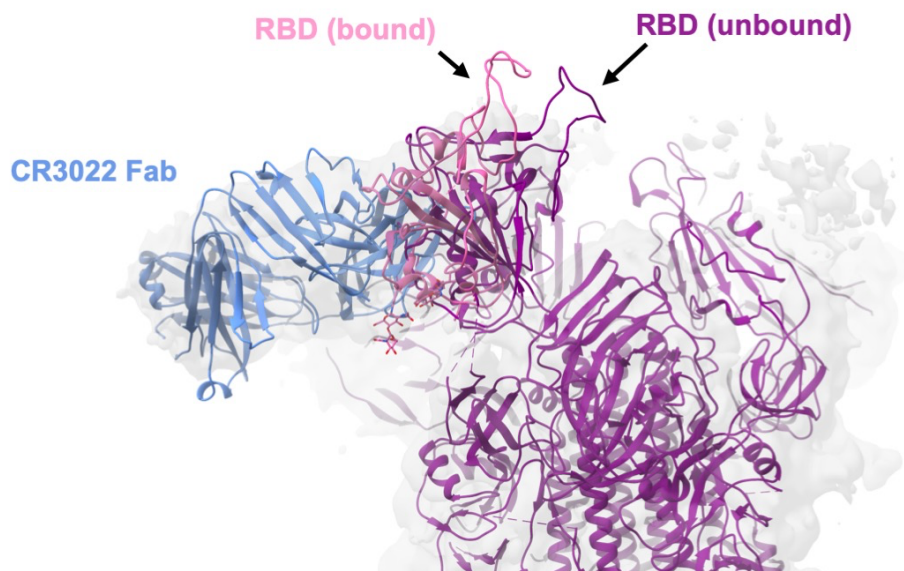
739

740 **Supplementary Figure 3. Representative cryo-electron micrograph and 2D class**
741 **averages of the SARS-CoV spike in complex with CR3022 Fab.** The top panel shows
742 a representative cryo-electron micrograph of the SARS-CoV spike complexed with
743 CR3022 Fab, whereas the bottom panels show the 2D class averages.



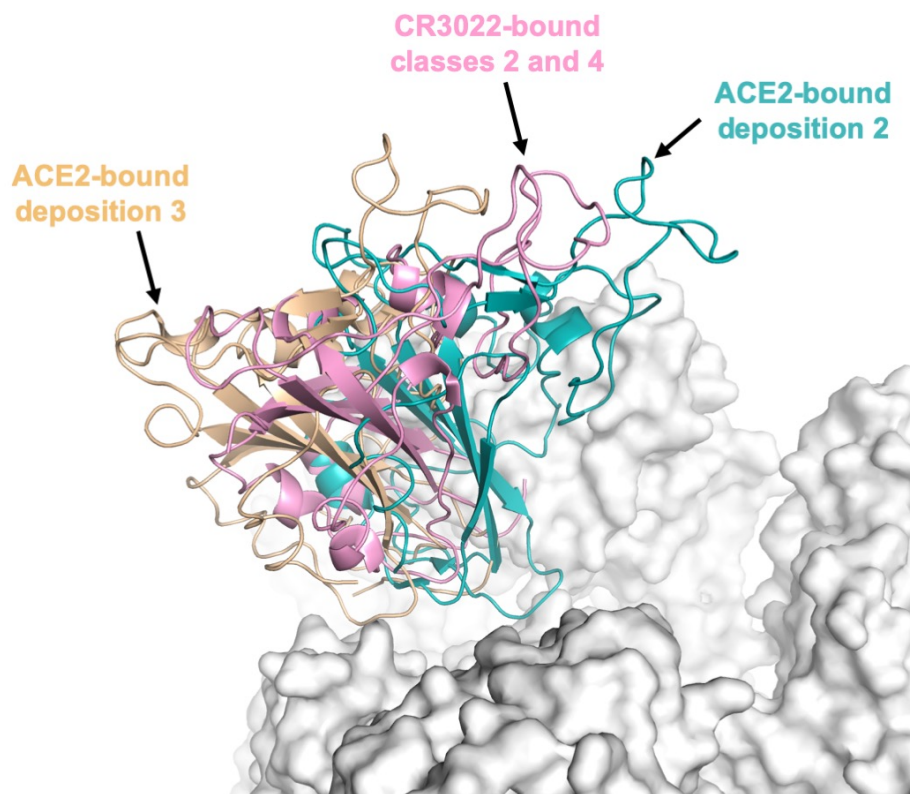
744

745 **Supplementary Figure 4. Workflow for cryo-EM data processing.** Four 3D class
746 averages of complex of the SARS-CoV spike and CR3022 were found during data
747 processing.



748

749 **Supplementary Figure 5. Comparison of conformations of CR3022-bound and**
750 **unbound RBDs.** The conformation of CR3022-bound RBD in class 2 and 4 is compared
751 to the conformation of RBD on an unliganded SARS-CoV S protein (PDB 6ACD) [35].



752

753 **Supplementary Figure 6. Comparison of conformations of CR3022-bound and**
754 **ACE2-bound RBDs.** The conformation of CR3022-bound RBD in class 2 and 4 is
755 compared to that of depositions 2 and 3 of ACE2-bound RBD (PDB 6ACJ and 6ACK,
756 respectively) [35].